Angewandte Chemie International Edition

Angewandte International Edition Chemie

How to cite: *Angew. Chem. Int. Ed.* **2026**, 65, e21654
doi.org/10.1002/anie.202521654

RESEARCH ARTICLE OPEN ACCESS

From Microscale to Nanoscale Shadow Electrochemiluminescence Microscopy

Xiaodan Gou[1,2] | Hanna Manko[3,4] | Jasmina Vidic[5] | Laurent Cognet[3,4] | Jun-Jie Zhu[2] | Neso Sojic[1]

[1]University of Bordeaux, Bordeaux INP, ISM, Pessac, France | [2]State Key Laboratory of Analytical Chemistry For Life Science, School of Chemistry and Chemical Engineering, Nanjing University, Nanjing, P. R. China | [3]University of Bordeaux, Laboratoire Photonique Numerique Et Nanosciences (LP2N), Talence, France | [4]LP2N, Institut d'Optique Graduate School &CNRS, Talence, France | [5]Université Paris-Saclay, INRAE, AgroParisTech, Micalis Institute, Jouy-en-Josas, France

Correspondence: Jun-Jie Zhu (jjzhu@nju.edu.cn) | Neso Sojic (sojic@u-bordeaux.fr)

Received: 3 October 2025 | **Revised:** 4 March 2026 | **Accepted:** 4 March 2026

Keywords: bioimaging | electrochemiluminescence | nanoscale microscopy | single entity | spores

ABSTRACT

Electrochemiluminescence (ECL) has emerged as a promising chemistry-based imaging technique, yet its potential in optical nano-imaging is still in the early stages. We report the label-free imaging of microobjects and nanoobjects with a sharp negative optical contrast. The shadow ECL images obtained are the optical signatures of the blocking of the electron-transfer reaction convoluted by the chemical reactivity and local diffusional hindrance of the ECL reagents by the object deposited on the electrode. Here, we address first the critical aspect of the smallest spherical nanoparticle imaged by shadow ECL microscopy. By investigating the imaging limits of shadow ECL, we demonstrate its capability to image single nanoparticles down to 50 nm. This work uncovers the sensitivity of the method by not only showing the smallest particles imaged by shadow ECL to date, but also, counterintuitively, a contrastive behavior of the single insulating particles with increased electrochemical rates at the insulator-electrolyte-electrode triple point. Finally, the practical utility of this shadow ECL method is illustrated by imaging complex samples such as densely packed particle assemblies or microbial *Bacillus subtilis* spores. It also opens new avenues for single-molecule and shadow ECL nano imaging of catalytic and biological systems.

1 | Introduction

For an optical imaging technique, exploring its imaging limits down to individual nanoobjects [1] not only demonstrates its potential but also serves as a critical milestone in driving the development of novel functionalities such as super-resolution methods [2, 3]. A long-standing belief was that single molecule sensitivity would be unattainable and that the Abbe diffraction limit represents an intrinsic resolution barrier for imaging [4]. However, single molecule detection over the past decades has enabled super-resolution microscopy techniques including stochastic optical reconstruction microscopy (STORM) [5], photoactivated localization microscopy (PALM) [6], points accumulation for imaging in nanoscale topography (PAINT) [7], and various derivative methods [8–19]. These technologies paved the way for nanoscopy and have revolutionized various fields such as biological imaging [6, 8, 11, 20, 21], nanomedicine [15], catalyst design [16], etc [22, 23]. Their theoretical basis lies in single-molecule localization methods [24]. Despite the constraints imposed by Abbe's limit, where even the smallest fluorescent molecules appear as diffraction-limited spots (i.e. Airy disks [25]), the ability to unambiguously detect and isolate the signal from a single fluorescent molecule enables increasingly precise localization of the emitter when imaging contrast increases [26, 27]. By controlling the emission states of individual fluorescent molecules and leveraging subsequently developed algorithmic models to achieve representation of the point spread function (PSF) [28], nano-imaging can thus be realized. One

of the most critical foundations in this field is ensuring that the photons emitted from a single molecule or nanoparticle are measured by the detector [26]. For nanoparticles, this often sets the smallest particle size that can be imaged by the fluorescence (FL) microscope, and thus impacts the precision of super-localization imaging techniques. Therefore, establishing the limit of sensitivity of a new optical technique when imaging sub-diffraction nanoparticles is essential for its development. Despite the remarkable progress of super-resolution FL microscopy, light excitation inherently introduces background FL interference, phototoxicity, and unavoidable photostability issues such as photobleaching under prolonged illumination.

Electrochemiluminescence (ECL), which generates photons from electrochemical reactions rather than from photoexcitation as in FL or phosphorescence, efficiently circumvents these issues [29]. In other words, it is intrinsically a chemistry-based microscopy, which differentiates it from physics-based microscopy as FL. The separation between the electrochemical excitation and light signal collection endows ECL with high sensitivity, rapid response, simple setup and inherent high spatiotemporal resolution when integrated with microscopy. Nowadays, ECL microscopy has been applied in various fields, including immunosensing [30–33], cell membrane imaging [34–36], sub-cellular entities [37–40], spheroids [41, 42], DNA responsive nanocarrier imaging [43], single protein imaging [44, 45], phase boundaries [46–50], dynamic chemical reactions [51–54], etc [51, 55–59]. Super-resolution ECL strategies have also emerged. Feng and coworkers [60, 61] achieved super-resolution ECL imaging based on single redox events combined with algorithmic reconstruction, enabling mapping the activity of gold nanoparticles [62], ultrasensitive immunoassays [63], and bacteria imaging [64]. Moreover, since ECL reflects the electrochemical activity of the substrate, another super-resolution strategy consists in employing analytical approaches [65] like the super-resolution radial fluctuations algorithm to narrow the PSF of individual catalytic sites, enabling sub-diffraction resolution imaging of single catalysts [66, 67]. Although single ECL events are intrinsically weak, most existing super-resolution ECL strategies operate in a positive imaging mode conceptually analogous to super-resolution FL microscopy, where emissive target are detected against a darker background [57, 68]. In these approaches, signal accumulation is achieved either by repeated photon emission from the same fluorophore (in FL) or by repeated electrochemical reactions occurring at the same spatial site (in single molecule ECL). However, in the latter case, diffusion effects may introduce additional challenges to quantitative accuracy, as both reactant transport (i.e. diffusion) and chemical dynamics can vary spatially and temporally.

In contrast, ECL uniquely enables an appealing negative imaging mode, which is termed as shadow ECL [39, 40, 69–75]. Introduced by Su and co-workers, this inherently label-free approach requires minimal sample preparation, and has been applied to fingerprint imaging [72, 73], cell-cell junction imaging [70], and even sub-cellular organelles imaging [39, 40], etc. In shadow ECL, freely diffusing luminophores produce a bright background, while target non-emissive objects locally hinder electron transfer and ECL reagent diffusion at the electrode surface, generating a "shadow" image (Figure 1a). In other words, shadow ECL microscopy is based on a clever spatial distribution of light and dark related to the local (electro)chemical activity. It presents some conceptual similarities with other FL label-free microscopies, where the cellular membranes block the diffusion of the free fluorophore [76–80]. While shadow ECL may superficially appear as a simple contrast inversion of the positive mode, its imaging capabilities are not inherently equivalent. It is a dynamic approach because it reflects the spatial distribution of the local diffusional fluxes of ECL reagents, which may be affected by objects blocking the initial electron-transfer reaction of the ECL process and/or with different permeability for the ECL reagents. Shadow signals may be masked by background luminescence from the diffusion of surrounding emitters. So far, systematic studies on minimal particle size that shadow ECL can resolve remain scarce.

In this work, we explore the spatial detection limits of shadow ECL imaging by integrating multi-frame averaging techniques allowing post-acquisition image enhancements and investigating the effects of surface reactivity, optical pathways, exposure time, reactant concentration, and even particle arrangement. We successfully achieve shadow ECL imaging of single particles at least as small as 50 nm and further extend it to the imaging of microbial spores using the model ECL system consisting of the freely-diffusing $[Ru(bpy)_3]^{2+}$ luminophore with the tri-*n*-propylamine (TPA) coreactant. The direct correlation between shadow ECL and FL signals demonstrates the accuracy and sensitivity of shadow ECL microscopy. In a first order approximation, the shadow ECL decrease (i.e. leading to image contrast) can be related to the fraction of the ECL reaction layer occupied locally by the object under investigation. The study of the sensitivity of shadow ECL allowing imaging sub-200 nm nanoparticles provides both theoretical and experimental foundations for the further methodological development of shadow ECL-based nano-imaging.

2 | Results and Discussion

To investigate the shadow ECL imaging sensitivity, we selected first spherical particles with sizes ranging from 6 μm down to 50 nm. Since ECL is initiated by an electrochemical trigger, it requires obviously an electrode surface. The electrode material may be either opaque or transparent such as a glassy carbon electrode (GCE) or an indium tin oxide (ITO) electrode, respectively. Both are extensively used in the ECL field [81].

The oxidation of TPA occurs efficiently on carbon-based material and it leads to bright ECL signals. However, the TPA oxidation is notably less efficient on standard ITO electrodes, giving a much lower ECL intensity compared to GCE. But both materials provide different benefits because they allow to perform ECL imaging experiments in different optical configurations. To extend the applications of shadow ECL-based approaches, the objects were imaged by shadow ECL microscopy in two optical configurations: i) in transmission on ITO electrodes (for the sake of clarity, denoted "ITO configuration"; Figures 1a and S1a) and ii) in reflection configuration with GCE electrodes (denoted "GCE configuration"; Figure S1b). The primary distinction between these two experimental configurations is the optical pathway. On one hand, due to the transparency of the ITO electrode material, imaging can be directly conducted beneath the sample and ECL light is transmitted through the electrode (Figure S1a). On the other hand, for the opaque GCE electrode, ECL emission

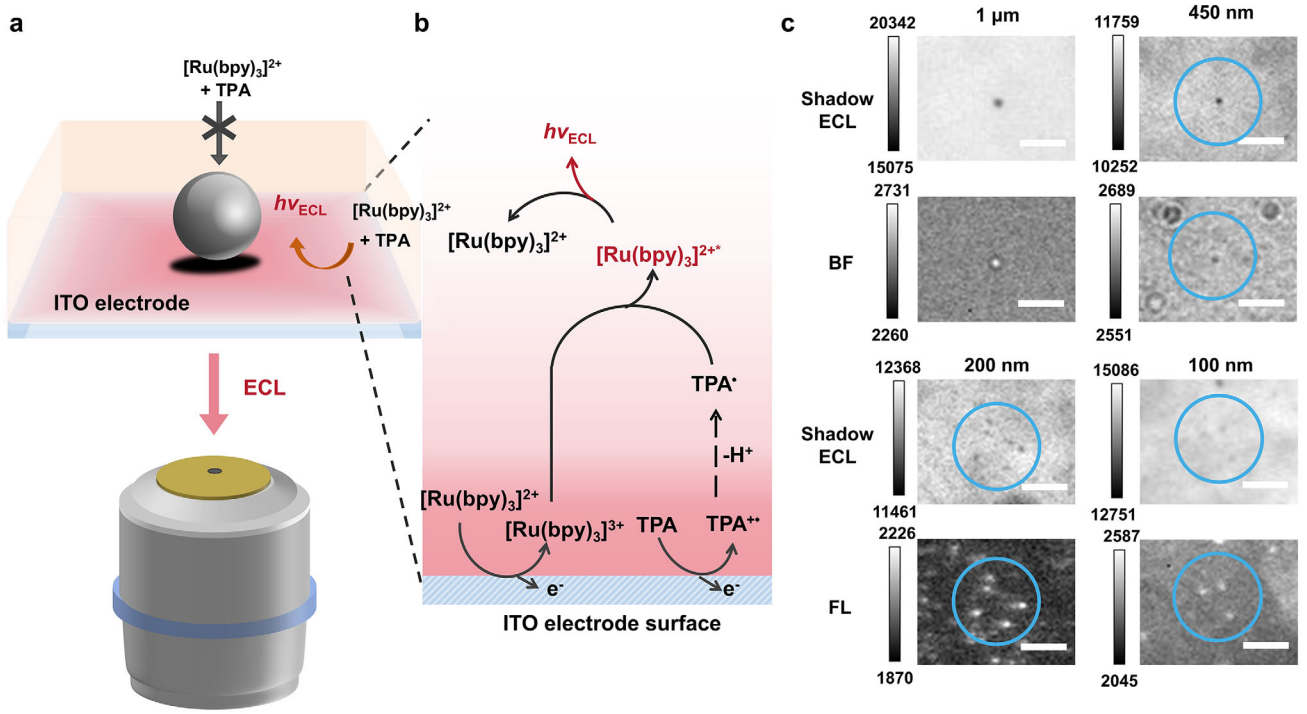

FIGURE 1 | (a) Scheme of shadow ECL microscopy for the ITO configuration operating in transmission mode with (b) the simplified ECL mechanism involving $[Ru(bpy)_3]^{2+}$ and TPA. (c) The shadow ECL and corresponding BF/FL images for different sizes of particles (1 μm, 450 nm, 200 nm, and 100 nm) on ITO. The blue circles facilitate the comparison between the shadow ECL and FL images. The electrolyte is 0.1 M PBS (pH = 7.4) containing 1 mM $[Ru(bpy)_3]^{2+}$ and 100 mM TPA. Applied potential: 1.2 V vs. Ag/AgCl. Exposure time: 500 ms. The shadow ECL images for 1 μm and 450 nm particles are an accumulation of 20 original bright shadow ECL images to improve the signal-to-noise ratio (SNR), while the shadow ECL for 200 nm and 100 nm is an accumulation of 50 and 120 images. Scale bars: 5 μm.

must be transmitted through the object and the solution under investigation before being collected by the microscope objective. Given that imaging targets—such as polystyrene (PS) beads, cells, and bacteria often exhibit some degree of transparency, this possibly may introduce some additional optical effects such as a lens effect [82–84] that influence the final imaging resolution. As shown in Figure 1a, 63× water-immersion objective is positioned below the transparent ITO electrode surface to record shadow ECL images in transmission mode. Typically, a potential of 1.2 V vs. Ag/AgCl was applied generating ECL emission on the entire ITO electrode surface except at the level of dark spots where particles were sedimented. A simplified mechanism generating the ECL emission is shown in Figure 1b. Single particles are clearly resolved by shadow ECL microscopy (Figure 1c). At the particle positions, heterogeneous electron transfer reaction and diffusion of ECL reagents are locally hindered, producing distinct dark spots against the bright ECL background. To confirm that these shadows correspond to the target particles, bright-field (BF), and FL images were recorded as references. For particles larger than 1 μm, BF and shadow ECL images showed perfect match. Although 450 nm silica beads remain visible in shadow ECL, their BF contrast becomes weak. For particles smaller than 450 nm, BF contrast is insufficient for accurate focusing; therefore, FL particles were used for validation. The spatial correspondence between FL and shadow ECL signals confirms that particles down to 100 nm are detectable. In addition, a slightly brighter ring surrounding the shadow of 3 μm beads (Figure S2) is observed, likely arising from enhanced electrochemical reaction rates [85], as discussed later.

However, when the particle size decreases to 50 nm (Figure S3), it becomes difficult to distinguish the particles in the FL image because FL is performed in presence of the $[Ru(bpy)_3]^{2+}$ luminophore in solution. The excitation and emission FL spectra of $[Ru(bpy)_3]^{2+}$ (Figure S4) exhibit an emission maximum around 620 nm and an excitation maximum near 465 nm, while maintaining relatively broad absorption below 500 nm. Although the fluorescent beads used in this study were selected to be spectrally as far as possible from the intrinsic background photoluminescence of the luminophore, the relatively broad bandwidth of the excitation light source with the limited FL dye doping in such small size results in elevated background signals in FL mode. Consequently, while the FL from the 50 nm particles can be collected, it does not provide sufficient contrast to serve as a reliable reference marker in all the experimental conditions. Despite this, at all positions where FL from 50 nm particles was detected, a corresponding negative shadow signal was consistently observed in the ECL mode (Figure S3b). Taken together, these results establish that shadow ECL reliably resolves ~100 nm particles and approaches its fundamental imaging sensitivity near 50 nm on ITO. Whatever, the spatial distribution of the FL spots follows the same pattern as the shadow ECL image (Figure 1c).

For the GCE setup, an inverted microscope was used to perform reflection shadow ECL imaging. As shown in Figure S5, under this configuration, 200 nm particles already approach the sensitivity limit. Only the large aggregates are seen when imaging 100 nm particles without signal post-enhancement techniques (see below and Figure S11). Notably, a lower luminophore

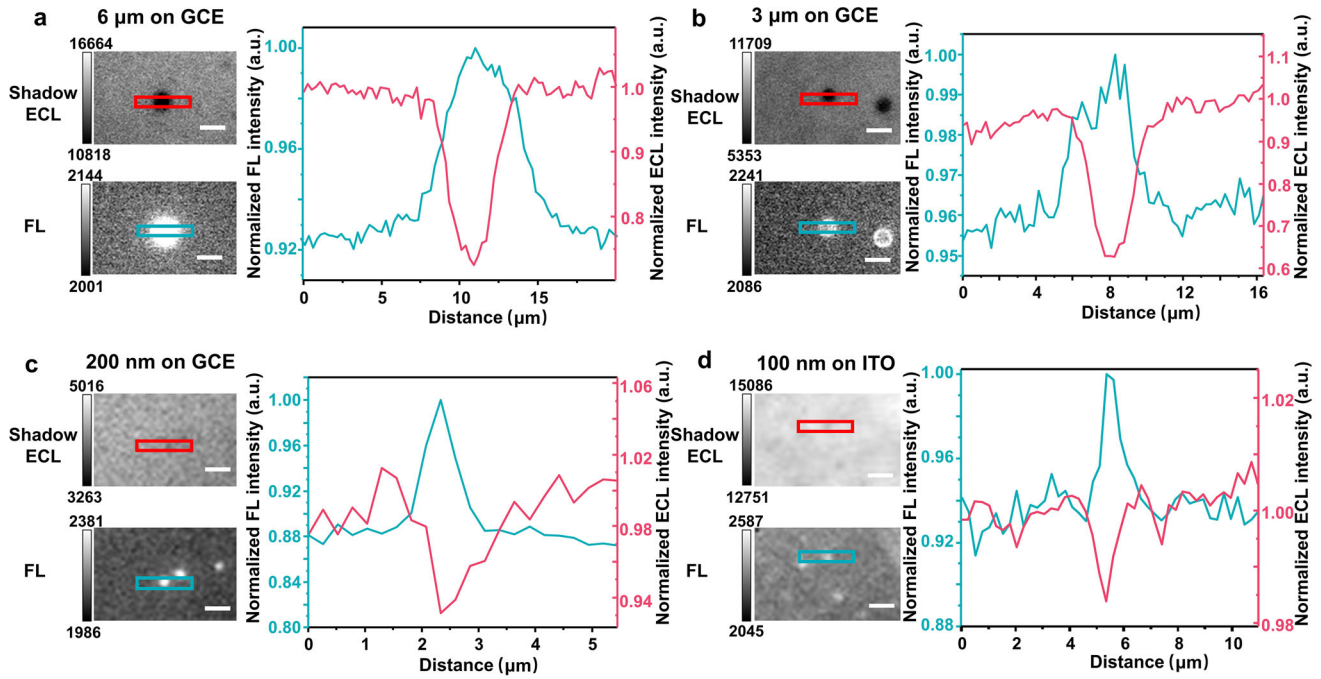

FIGURE 2 | Shadow ECL and FL images of (a) 6 μm, (b) 3 μm, (c) 200 nm, and (d) 100 nm beads recorded in the (a–c) GCE or (d) ITO configuration. Corresponding normalized shadow ECL (red) and FL (green) intensity profiles extracted along the ROI from the shadow ECL and FL images. Scale bars: (a, b) 5 μm and (c, d) 2 μm. Exposure times: (a, d) 500 ms, (b) 1 s, (c) 200 ms. The image is obtained by averaging (a, b) 5, (c) 50, and (d) 120 original images to obtain a better SNR. For the experiments in the GCE configuration (a, c), the Procell solution contained 30 μM $[Ru(bpy)_3]^{2+}$. For the experiments in the ITO configuration (d), the PBS solution contained 1 mM $[Ru(bpy)_3]^{2+}$ and 100 mM TPA solution. Same applied potential for (a-d): 1.2 V vs. Ag/AgCl.

concentration (30 μM) was employed for GCE due to the higher oxidation efficiency of TPA on its surface [86], as excessive concentrations possibly lead to the signal saturation. In a 16-bit image, grayscale values (ranging from 0 for pure black to 65,535 for pure white) encode pixel brightness, directly correlating with FL or ECL intensity. We utilized an electron-multiplying charge-coupled device (EMCCD) for ECL signal detection, because its unique gain register amplifies the weak signals, enabling single-photon events to span hundreds of grayscale levels. This property is critical for the weak-light system such as ECL and thus the electrochemical efficiency and reagents concentrations are essential factors. To determine the smallest detectable particle size (i.e. the sensitivity), we compared the normalized intensity profiles of shadow ECL and FL for particles of different sizes (Figure 2). We first examined the intensity profiles of larger particles on GCE (Figure 2a and b, corresponding to 6 and 3 μm particles, respectively) and observed that the FL intensity peak aligns well with the shadow ECL intensity minimum, confirming the spatial correspondence of shadow ECL signals with the position of the particles. Similarly, for smaller objects (200 nm on GCE and 100 nm on ITO, Figures 2c and 2d), discernible shadow profiles matched FL intensity distributions, further proving the shadow ECL are indeed caused by the nanoparticles obstructing the electrochemical reactions on the electrode surface.

In order to further quantify the variation in shadow ECL intensity profiles, we introduce the decrease shadow ECL ratio, providing a metric to assess the shadow ECL imaging sensitivity:

$$\text{decrease shadow ECL ratio} = \frac{I_{\text{average}} - I_{\text{shadow}}}{I_{\text{average}} - I_{\text{offset}}}$$

In the given equation I_{average} indicates the average ECL intensity in the bare electrode region. I_{shadow} represents the ECL intensity in the shadow region, and I_{offset} represents the intrinsic signals of the EMCCD. As shown in Figure 3, the decrease ratio for the ITO configuration exhibits a near-linear relationship with particle sizes ranging from 3 μm to 100 nm. Within this range, a linear fit between the decrease ratio and particle diameter yields the equation $y = -0.0049 + 0.1333\,x$, with an R^2 value of 0.992 (Figure S6). In contrast, the GCE setup shows larger variations and standard deviations. In a first order approximation, this linear trend can be explained by the fraction of the ECL reaction layer that is perturbed by the object under investigation. However, it is very difficult to simulate because it involves several experimental parameters and physicochemical effects: i) the hindrance of the diffusion flux of the ECL reagents by the insulating objects, ii) the ECL mechanism, which depends on the electrode material (ITO or GC) and the concentrations of the ECL reagents, iii) the thickness of the ECL emitting layer, iv) the spatial distribution of the emitted ECL intensity with the distance from the electrode surface, v) the influence of enhanced electrochemical reaction rates at the triple insulator-electrolyte-electrode point (vide infra), etc. Whatever, a linear-relationship suggests that the imaging system responds uniformly to different particle sizes, meaning its detection sensitivity remains consistent across various scales without significant nonlinear distortions (such as saturation effects or background noise interference). Thus, it further proves that the imaging sensitivity of ITO is sufficient to approach at least 100 nm particles. It should also be noted that for the 50 nm particles in the ITO configuration, the measured decrease ratio does not deviate significantly from the initial linear trend. When the 50 nm data point is included in the fit, the resulting linear

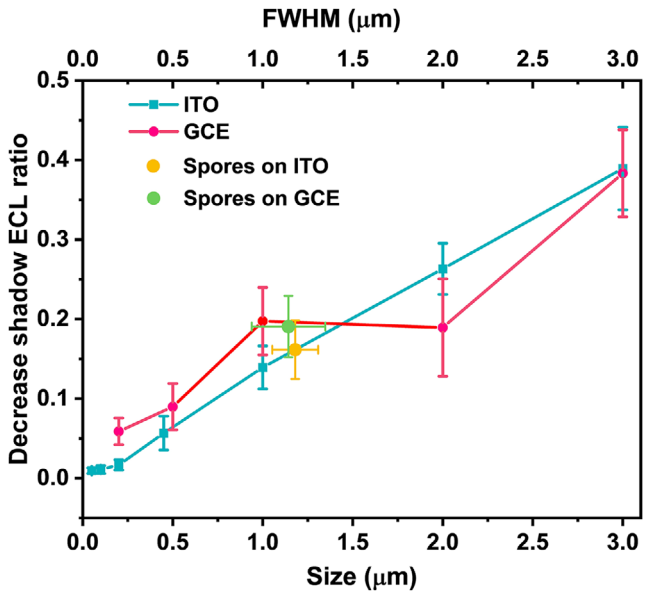

FIGURE 3 | Evolution of the decrease shadow ECL ratio as function of the particle (PS beads or spores) size in both ITO and GCE configurations. The blue squares and red dots show the decrease ratio for the PS beads in ITO and GCE configurations, respectively. The yellow and green dots represent the relationship between the decrease ratio for spores and their sizes on the ITO and GCE configurations, respectively. The size of the spores is expressed in terms of FWHM. For the data point presented for each particle and spore, $n = 20$. Error bars represent the standard deviation.

relationship yields an R^2 value of 0.978 (Figure S7), which remains high. This result further supports the capability of shadow ECL to image particles down to this size regime. In contrast, the decrease ratio on GCE shows a similar trend but with a higher variability due to the experimental configuration used. Moreover, although different numbers of frames were averaged for some particles of different sizes, the number of averaged frames has only a negligible effect on the decrease ratio of individual particles (see Figure S8 for details).

Next, to investigate further the imaging capabilities of the reported approach, we extracted the full width at half maximum (FWHM) from FL, shadow ECL and post-enhanced shadow ECL profiles for different particle sizes by 1D and 2D Gaussian fitting (Figure S9). Compared with FL, shadow ECL generally exhibits smaller FWHM values due to its intrinsically surface-confined nature. By incorporating more spatial information, 2D Gaussian fitting provides a more reliable description when particle size approaches the imaging limit (see detailed discussion on FWHM in Figure S9). Importantly, breakdown of FWHM scaling at 100–200 nm does not imply imaging failure, which highlights the distinction between detectability and apparent image width.

Except the setup itself, several additional factors should also be considered to influence the imaging limits including: i) image processing method (multi-frame averaging, contrast enhancement and denoising), ii) exposure time, iii) reactant concentration, and iv) the stacking arrangement of targets. Notably, the shadow ECL images showed here are not generated by the single capture but by averaging multiple frames. As shown in Figure S10, for 100 nm particles on ITO, the single image with 500 ms exposure time fails to resolve the shadow signal due to the low signal-to noise-ratio (SNR). The SNR is defined as [87]:

$$\mathrm{SNR} = \frac{S}{\sigma}$$

where S represents the signal intensity, and σ represents the noise standard deviation. For small particles, the signal is easy to be overwhelmed by random noise, which mainly includes three types listed as follows [88–90]: 1) Thermal noise of the detector, which is generated by the thermal motion of electrons. 2) Readout noise of the detector, which is introduced by circuit interference during signal digitization. 3) Shot noise of the emitted photons (Poisson noise), which arises due to the discrete nature of photons and their random arrival times at the detector. Multi-frame averaging effectively improves SNR because the signal accumulates across frames, whereas random noise remains statistically uncorrelated. As a result, stacking N frames enhances the SNR by $\sqrt{N}$ (derivation provided after Figure S10) [91]. Accordingly, the shadow signal of 100 nm particles becomes distinguishable after averaging approximately 50 frames (Figure S10).

Interestingly, multi-frame acquisition can be used to analyze noise statistics and further improve SNRs by denoising algorithms. Here, two representative post-processing approaches, deconvolution, and deep-learning-based denoising, were applied to shadow ECL images acquired near the imaging limit. When particle size approaches 100–200 nm, the shadow contrast becomes extremely weak and is further blurred by the optical PSF. PSF-based deconvolution (Fiji, Richardson–Lucy algorithm; see Supporting Information for details) partially compensates for this blur and improves visual sharpness (Figures 4 and S11, deconvolution). Moreover, it can also partially compensate for small z-axis drift, making the image closer to that acquired at optimal focus. Yet, caution is required as excessive iterations can lead to overfitting of noise, causing the particle shadow to be obscured again by background fluctuations. Next, the contrast of the shadow ECL images was enhanced using Fast Fourier Transform (FFT)-based band-pass filtering, followed by the application of Noise2Self, a self-supervised image denoising algorithm (see Supporting Information for details). FFT-based filtering plays a major role in improving the visual appearance of the images, while using Noise2Self can improve the SNR to some extent without introducing artificial structures. As shown in the Figures 4, S11, and S12, the post enhanced images of nanoparticles exhibit a substantial improvement in visual contrast. For example, the normalized intensity profile of a 50 nm particle shows a significantly enhanced shadow contrast after post-processing (Figure S12b). However, pixel intensities in processed images no longer represent absolute ECL intensities but algorithm-modified values for contrast enhancement. Therefore, physically meaningful parameters such as the decrease ratio are evaluated using raw images. It should also be highlighted that these post-processing methods are auxiliary tools applied only after shadow ECL has already successfully detected nanoscale particles. Post-processing enhances visual clarity, but it cannot recover structural information that is not present in the raw data. As shown by Figure 4, individual 100 nm shadow ECL features

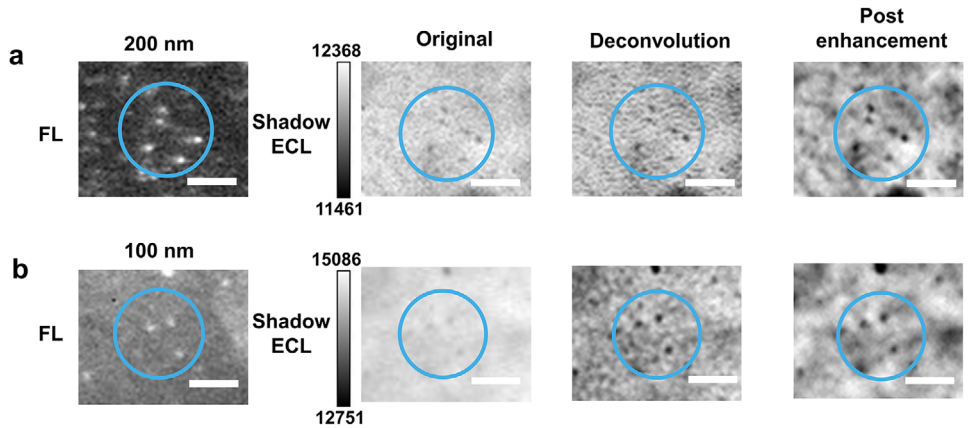

FIGURE 4 | From left to right: corresponding FL images, original shadow ECL images with the number of averaged frames that has been described before, shadow ECL images obtained after deconvolution, and the post enhanced images using FFT-based bandpass filtering and Noise2Self algorithm for (a) 200 nm and (b) 100 nm particles on ITO. The electrolyte is 0.1 M PBS (pH = 7.4) containing 1 mM $[Ru(bpy)_3]^{2+}$ and 100 mM TPA. Applied potential: 1.2 V vs. Ag/AgCl. Scale bars: 5 μm.

are clearly visible after post-processing and aggregated regions (yellow-circled) display improved contrast (Figure S11c).

Although multi-frame averaging markedly improves SNR, increasing frame number does not indefinitely enhance shadow ECL contrast. Comparison between 50-frame and 120-frame averages reveals negligible differences in both intensity profiles (Figure S13) and structural similarity index (Figure S14, SSIM = 0.993), indicating that sufficient SNR is already achieved at intermediate frame numbers. Excessive averaging increases computational demand and prolongs acquisition time, making the system more susceptible to instrumental drift, particularly along the z-axis direction. Moreover, the choice between multi-frame averaging and single long exposure requires careful consideration. In principle, extending exposure time increases the number of collected photons and can improve SNR, particularly when readout noise and shot noise dominate (see detailed discussion after Figure S15). However, in practice, long exposure does not necessarily yield better shadow contrast. As shown in Figure S15a, the image obtained with a 5 s exposure time appears less distinct compared to an image generated by averaging 10 frames with a 500 ms exposure (Figure S15b) even though the total detecting time is the same. This is because long exposure also introduces other uncertainties. Background accumulation increases shot noise, and high-intensity regions may approach saturation, reducing contrast in weak shadow areas. More critically, axial (z-axis) drift becomes difficult to manage during long exposures. Although lateral (xy) drift remains minimal under our experimental conditions, as confirmed by pre- and post-imaging overlays and drift correction analysis (detailed discussion after Figures S16 and S17), small axial drift caused by thermal or mechanical fluctuations leads to defocusing effects (Figure S18). Minor z drift can be partially mitigated by deconvolution, but significant defocus cannot be corrected algorithmically. Under short-exposure conditions, z drift can be promptly identified and compensated by refocusing; however, during long exposures the lack of real-time feedback makes such correction difficult, rendering z drift a more significant limitation. Nevertheless, excessively short exposure is also unfavorable. As shown in Figure S15b, 50 ms exposure failed to reveal shadow features even after averaging 200 frames, likely because critical details in dark regions are lost within noise in individual frames and cannot be recovered by stacking. Therefore, an optimal balance between exposure time and frame number is essential for reliable shadow ECL imaging.

Since the ECL generation relies on the electrochemical reactions, the factors influencing reaction kinetics, such as the concentration of the reagents, should be taken into consideration. On ITO, decreasing the luminophore concentration to 30 μM markedly attenuated the ECL emission, requiring long exposures (e.g., 10 s) to collect sufficient photons. Under this condition, 6–2 μm PS beads remained detectable, but the images exhibited higher background noise and the long exposure time made multi-frame averaging impractical (Figure S19). For 1 μm beads, the shadow became difficult to distinguish even with a 30 s exposure time. Consistently, the decrease ratio at 30 μM was lower than that at 1 mM $[Ru(bpy)_3]^{2+}$ (Figure S19b), indicating a weaker contrast between the shadow region and background. It is noted that in Figure S19b, the relatively high decrease ratio observed for the 3 μm beads at a luminophore concentration of 1 mM is most likely attributed to the accelerated electrochemical reaction at the three-phase boundary, which will be discussed in detail later. Since this effect is volume-dependent, it can lead to a lower decrease ratio for the larger 6 μm beads. In contrast, this trend is not evident on ITO at 30 μM, most likely because the weak emission reduces contrast and masks the three-phase-boundary contribution.

Similarly, we also tested both higher and lower $[Ru(bpy)_3]^{2+}$ concentrations on GCE setup (1 mM, Figure S20; 600 nM, Figure S21a–c.) At 1 mM, careful tuning is required to avoid partial saturation/overexposure. Despite the higher ECL intensity, 200 nm particle imaging still failed, demonstrating that simply increasing the ECL intensity does not necessarily push the imaging sensitivity. When the concentration was reduced to 600 nM, single-frame images of 500 nm beads were difficult to discern (Figure S21a). However, due to the higher ECL efficiency on GCE, sufficient photons could still be collected with shorter exposures by adjusting EMCCD gain, enabling multi-frame averaging. As shown in Figure S21c, 500 nm beads became detectable

after averaging 50 frames, whereas 200 nm particles still could not be resolved as individual shadows and mainly appeared as larger aggregates. This limitation likely arises from rapid ECL decay in the confined reaction volume near GCE surfaces, further diminishing the imaging quality of multi-frame averaging. Comparing decrease ratios across concentrations (Figure S21d), the values at 1 mM on GCE are relatively lower. One possible explanation is that at this higher luminophore concentration, the ECL reaction layer becomes thicker [70, 92]. For larger particles, this reaction layer thickness may not significantly affect imaging—even if the decrease ratio is lower, the shadow signal remains distinguishable. However, for 200 nm particles, this increased thickness may mask the shadow signal, ultimately causing the limit in nanoparticle imaging discrimination. Owing to the superior electrochemical activity of the GCE, even at a luminophore concentration of 600 nM, sufficiently strong ECL emission can be obtained without requiring long exposure times (e.g., ≥10 s). As a result, the three-phase boundary–induced acceleration effect is still reflected in the decrease shadow ECL ratio under this condition, manifested by a higher decrease ratio for the 3 μm beads. When the luminophore concentration is increased to 1 mM, the ECL emission on the GCE appears to become excessively strong, leading to an increased ECL layer thickness and partial image saturation. These effects may then mask the contribution of the three-phase boundary–accelerated electrochemical reactions to the decrease ratio. Overall, the trend of the decrease ratio in this case is relatively complex, as it arises from the combined influence of image quality, three-phase boundary acceleration effects, and variations in the ECL emission layer thickness.

When discussing the imaging limit, the focus is often placed on the ability to observe smaller particles. While this is reasonable, certain implicit factors may be overlooked, such as the influence of enhanced electrochemical reaction rates at the triple point (insulator-electrolyte-electrode) [85, 93] on shadow ECL imaging, which we aim to highlight here. Ciampi and co-workers reported that insulating fouling on electrodes induces locally accelerated electrochemical reactions, attributed to TPA adsorption and current crowding at the triple point. Recently, they imaged by ECL the enhancement of the mass transport by electrode fouling, due to electrochemically actuated lateral density gradients [93]. In our study, a similar effect is observed at much smaller scales (3 and 6 μm PS particles; Figures S22 and S23). A characteristic bright ring appears around the shadow region, more pronounced for 6 μm particles, consistent with enhanced mass transport and adsorption near larger insulating objects. This phenomenon is general and observed on both ITO and GCE.

According to Ciampi's findings, this bright-ring enhancement may become more prominent over time. To quantify this effect, we defined an enhancement factor (EF) and compared the time evolution of ECL intensities in the particle and in the background region from 1 s, 5 s to 10 s under single-frame 500 ms exposures (Figure S24 for 3 μm particles and Figure S25 for 6 μm particles, respectively).

$$\text{enhancement factor} = \frac{I_{\max} - I_{\text{offset}}}{I_{\text{background}} - I_{\text{offset}}}$$

$I_{\max}$ refers to the maximum ECL intensity within the particle region marked by the orange circle, while $I_{\text{background}}$ refers to the average ECL intensity within the background region marked by the green circle in Figures S24 and S25. The definition of I_{offset} is the same as before. Grayscale intensity distributions extracted from ROIs (Figures S24 and S25) show that blank regions follow near-Gaussian distributions, whereas particle regions exhibit broader distributions due to the coexistence of bright-ring and shadow pixels. With increasing particle size, the distribution of the bright ring approaches Gaussian behavior, consistent with less affected by stochastic fluctuations in larger pixel areas. However, EF for both 3 and 6 μm particles on ITO shows only a slight decrease over 10 s (Figure S26). This is possible for several reasons: (1) the experiments were conducted in a near-neutral buffer (pH = 7.4), where $[Ru(bpy)_3]^{2+}$/TPA systems generally show the highest emission [94], and the ITO electrode configuration permits enough space for solution reaction and diffusion, therefore, no obvious ECL decay was observed within 10 s; (2) the particle sizes imaged here are still much smaller than those reported in the previous study, thus limiting the enhancement effect. In contrast, ECL on GCE decayed more rapidly. We further analyzed the grayscale histograms and EF evolution within 5 s for 6 μm PS particles on GCE (Figures S27 and S28). Because the overall brightness was lower, the particle and background grayscale distributions nearly overlapped; nevertheless, the EF demonstrated that the enhancement at the triple point persisted even under rapidly decaying ECL backgrounds.

We further examined the influence of exposure time (50 and 500 ms), frame averaging (to minimize temporal effects, images with 50 and 500 ms exposure times were averaged over 200 and 20 frames), and luminophore concentration (30 μM) on this enhancement effect (Figures S29–S31). Overall, the enhancement is consistently stronger for 6 μm than for 3 μm particles (Figure S32). Single-frame 50 ms images yield the highest EF values, likely due to stochastic photon fluctuations artificially elevating intensity peaks. Longer exposures (500 ms) provide better histogram separation between particles and background but slightly lower EF. After multi-frame averaging, the histogram differences were further accentuated. And it also reduced the EF, which may be attributed to mild ECL decay during extended acquisition time and smoothing of abnormally high-intensity pixels. When the luminophore concentration was reduced to 30 μM (Figure S31) while keeping the TPA concentration constant, the relative proportion of TPA increased. Since adsorption of TPA is one origin of the enhancement effect, the EF should increase under these conditions. Moreover, since the long exposure time was acquired to obtain enough emission, multi-frame averaging could not be performed. As a result, the grayscale histograms of particle and blank regions tended to overlap. The final results were consistent with our prediction.

Undoubtedly, this enhancement effect influences shadow ECL imaging. Notably, the decrease ratio of 6 μm particles is lower than that of 3 μm particles on both ITO and GCE (Figure S33), deviating from simple geometric scaling. Similarly, FWHM differences between the shadow ECL of 6 and 3 μm particles are smaller than those between 3 and 2 μm particles (Figure S9a), likely due to the mass transport at the bright ring that influence the area of shadow region. These findings raise an important question: whether a

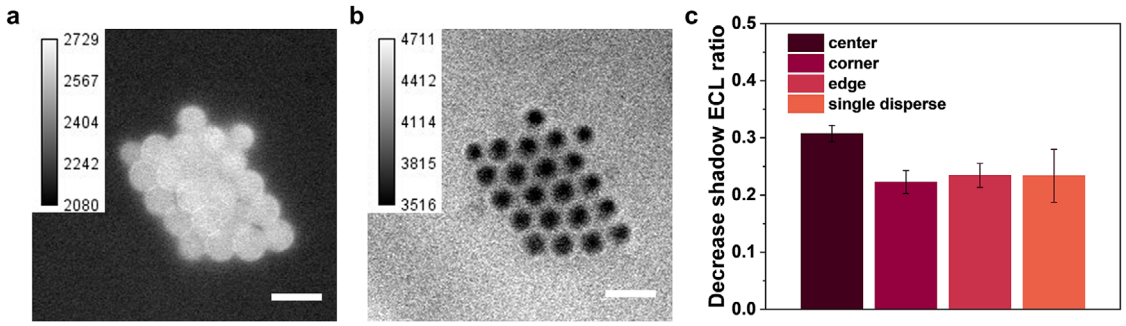

FIGURE 5 | Influence of bead stacking on shadow ECL imaging. (a) FL and (b) shadow ECL images of an assembly of densely packed 6 μm particles. Same experimental conditions as in Figure 2 with the GCE configuration. Scale bar: 10 μm. Exposure time: 500 ms. The shadow ECL image is obtained by overlaying five original images to obtain a better SNR. (c) Comparison of decrease shadow ECL ratio for different locations of particles: center of the stacking, corner particles and edge particles in (b) and other single isolated particles ($n = 6$ for center, $n = 5$ for corner, $n = 11$ for edge, and $n = 20$ for single isolated particles.) Error bars represent the standard deviation.

similar triple-point enhancement effect exists at the nanoscale and may partially mask shadow contrast near the imaging limit.

Since the target PS particles are spherical, a 200 nm diameter particle has a very limited contact area with the electrode surface. The effective contact diameter is likely less than 200 nm. Such a small contact area is easy to be disguised by the background interference. This distinction between overall particle size and effective contact dimension is supported by the comparison of FL and shadow ECL FWHM (Figure S9), where shadow ECL consistently yields smaller values, reflecting surface contact rather than total particle size. These observations raise an intriguing question whether particle shape (e.g., square particles, where the particle size and contact diameter should theoretically be more consistent) or packing—by increasing effective contact area could improve shadow ECL detectability for even smaller objects.

To answer this question, we investigated more complex entities by shadow ECL (i.e. tightly packed cluster of 6 μm particles) on GCE (Figure 5). The bead ensemble (~30 beads) exhibits strong overlap in FL images due to mutual compression and multilayer stacking (Figure 5a). In contrast, shadow ECL revealed 22 well-resolved individual shadow spots (Figure 5b), corresponding to beads in direct contact with the electrode. consistent with the surface-confined nature of ECL [35]. As shown in Figure 5c, centrally located beads display higher decrease ratios than peripheral ones. Indeed, in the central region, the tight packing not only caused some deformation, but also hindered more the diffusion of luminophores compared to the peripheral ones. Here, the peripheral regions include both corner particles and edge particles. We define corner particles as those with a larger contact area with the solution, which may be influenced more by the diffusion of surrounding luminophores, leading to a relatively lower decrease ratio. However, when comparing the corner particles with the edge and individually dispersed particles, the difference is not significant. But still, the higher decrease ratio in the central part further demonstrates that particle packing influences shadow ECL imaging performance.

We have already demonstrated that shadow ECL is capable of imaging nanoscale particles or ensembles, but its utility in practical microbiological imaging remains to be explored. Here, *Bacillus subtilis* spores were imaged after sedimentation on ITO and GCE. A typical spore has a length of ~1.3 μm and a width of ~820 nm as confirmed by SEM (Figure S34). The spores possess intrinsic FL, enabling direct comparison. Shadow ECL successfully resolves individual spores on both substrates (Figure 6a and c), with strong spatial correspondence to FL images. Representative FL and shadow ECL intensity profiles of a single spore (Figure 6b and d for GCE and ITO configurations, respectively) further confirm this agreement, underscoring the practicality of shadow ECL as a label-free technique. For both ITO and GCE electrodes, the post-processed images of spores also exhibit improved contrast with enhanced visual clarity (Figure S35). Statistical analysis of decrease ratio vs. spore size (yellow dots for ITO, green for GCE in Figure 3) reveals a well-defined linear relationship (here, the size of spores was represented by their FWHM). It also demonstrates the consistency of the decrease ratio of spores with that of particles around 1 μm in size. This good agreement between the relationship of decrease ratio and sizes also corroborates the accuracy of shadow ECL imaging for biological application.

3 | Conclusion

In summary, we have demonstrated the potential of shadow ECL as a label-free, simple, and effective imaging technique for visualizing extremely small particles down to the nanoscale. We systematically investigated the effects of multi-frame averaging, exposure time, surface reactivity, post-acquisition image enhancement, and optical configuration on imaging quality and revealed the influence of luminophore concentration on shadow ECL imaging. Insufficient luminophore concentration leads to reduced ECL intensity, making it difficult to distinguish shadow ECL signals from background noise, whereas excessively high concentrations increase the ECL reaction layer thickness, potentially masking shadow ECL of small particles. Under optimal conditions (1 mM $[Ru(bpy)_3]^{2+}$ and 100 mM TPA for ITO setup), we demonstrated that shadow ECL can achieve imaging sensitivities down to 50 nm particles. In addition, we conducted a detailed discussion on the impact of increased electrochemical rates at the insulator–electrolyte–conductor boundary on shadow ECL imaging, demonstrating that this phenomenon may hinder the imaging limit of shadow ECL. We also found that denser

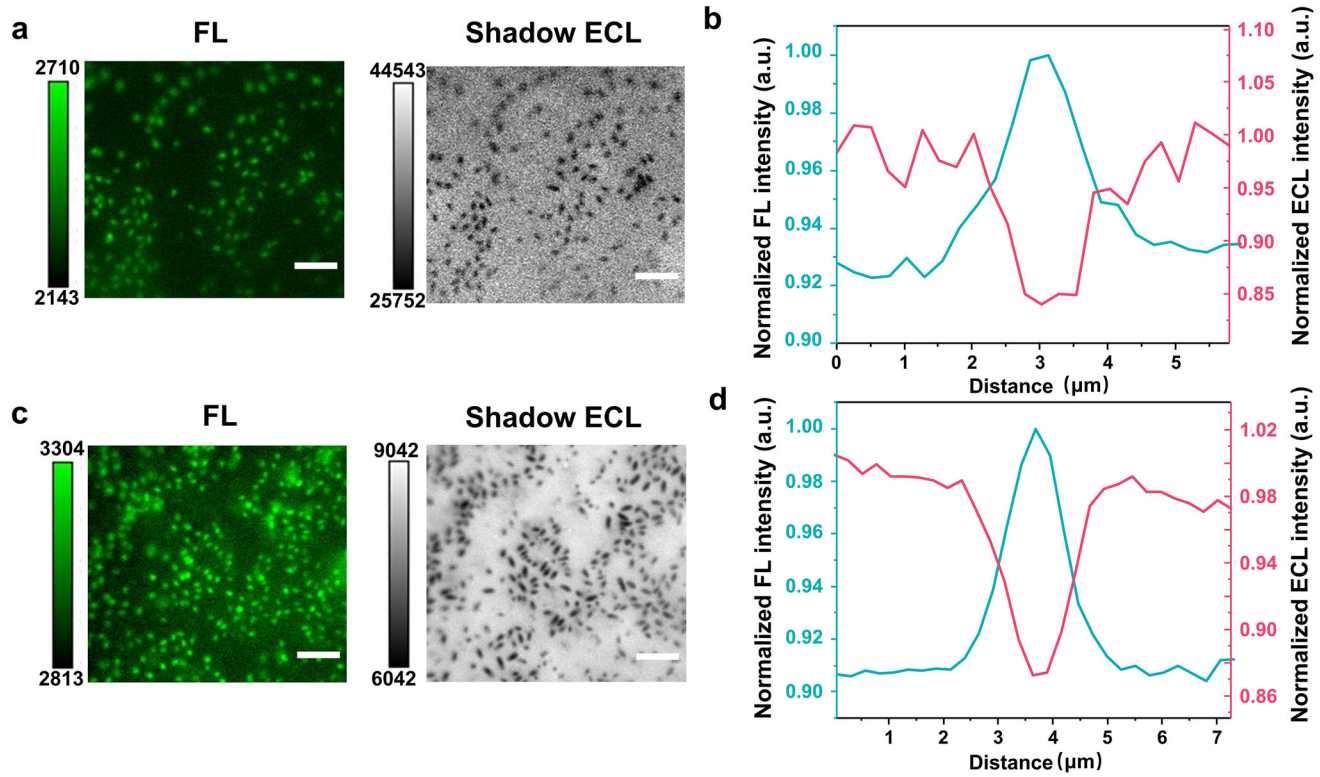

FIGURE 6 | FL and shadow ECL images of spores in the (a) GCE or (c) ITO configuration. The shadow ECL images were obtained by overlaying (a) 5 or (c) 20 original images to obtain a better SNR. (b, d) A typical normalized FL and shadow ECL intensity profiles of a single spore in both configurations. Same experimental conditions as in Figure 2. Exposure time: (a) 1 s and (c) 500 ms. Scale bar: 10 μm.

particle packing could facilitate the imaging limit. Finally, the shadow ECL was successfully applied to image spores with high image quality, which highlights the practical potential of shadow ECL in microbial imaging applications.

The unique negative-mode imaging mechanism of shadow ECL eliminates the need for labeling and its capability to detect nanoparticles below the Abbe diffraction limit has been validated. This provides a theoretical foundation for shadow ECL based nanoscopy. Given the widespread applications of shadow ECL imaging in electrode-interface dynamics and single entity imaging, we anticipate that super-resolution shadow ECL will contribute to high spatiotemporal resolution and high-specificity imaging, bringing new opportunities for advanced imaging technologies.

Acknowledgements

This work was supported by the China Scholarship Council, the European Union (Grant agreement No. 101135402, Mobiles project), the Agence Nationale de la Recherche (2PhotonECL—ANR-23-CE06-0024-02), the Program for Outstanding PhD candidates of Nanjing University (2025A03), the European Research Council to LC (Synergy grant 951294), and the Idex Bordeaux (Grand Research Program GPR LIGHT). We also acknowledge the helpful discussions with Prof. Simone Ciampi.

Open access publication funding provided by COUPERIN CY26.

Conflicts of Interest

The authors declare no conflicts of interest.

Data Availability Statement

The data that support the findings of this study are available from the corresponding author upon reasonable request.

References

1. W. E. Moerner and M. Orrit, "Illuminating Single Molecules in Condensed Matter," *Science* 283 (1999): 1670–1676, https://doi.org/10.1126/science.283.5408.1670.

2. J. Biteen and K. A. Willets, "Introduction: Super-Resolution and Single-Molecule Imaging," *Chemical Reviews* 117 (2017): 7241–7243, https://doi.org/10.1021/acs.chemrev.7b00242.

3. P. Bon and L. Cognet, "On some Current Challenges in High-Resolution Optical Bioimaging," *ACS Photonics* 9 (2022): 2538–2546, https://doi.org/10.1021/acsphotonics.2c00606.

4. E. Abbe, "Beiträge zur Theorie des Mikroskops und der Mikroskopischen Wahrnehmung," *Archiv für Mikroskopische Anatomie* 9 (1873): 413–468.

5. M. J. Rust, M. Bates, and X. Zhuang, "Sub-diffraction-limit Imaging by Stochastic Optical Reconstruction Microscopy (STORM)," *Nature Methods* 3 (2006): 793–796, https://doi.org/10.1038/nmeth929.

6. E. Betzig, G. H. Patterson, R. Sougrat, et al., "Imaging Intracellular Fluorescent Proteins at Nanometer Resolution," *Science* 313 (2006): 1642–1645, https://doi.org/10.1126/science.1127344.

7. A. Sharonov and R. M. Hochstrasser, "Wide-field Subdiffraction Imaging by Accumulated Binding of Diffusing Probes," *Pnas* 103 (2006): 18911–18916, https://doi.org/10.1073/pnas.0609643104.

8. H. Deschout, T. Lukes, A. Sharipov, et al., "Complementarity of PALM and SOFI for Super-resolution Live-cell Imaging of Focal Adhesions," *Nature Communications* 7 (2016): 13693, https://doi.org/10.1038/ncomms13693.

9. Y. Yang, Y. Ma, J. F. Berengut, et al., "Electrochemically Controlled Blinking of Fluorophores for Quantitative STORM Imaging," *Nature Photonics* 18 (2024): 713–720, https://doi.org/10.1038/s41566-024-01431-0.

10. M. Bowler, D. Kong, S. Sun, et al., "High-resolution Characterization of Centriole Distal Appendage Morphology and Dynamics by Correlative STORM and Electron Microscopy," *Nature Communications* 10 (2019): 993, https://doi.org/10.1038/s41467-018-08216-4.

11. B. Dudok, L. Barna, M. Ledri, et al., "Cell-specific STORM Super-resolution Imaging Reveals Nanoscale Organization of Cannabinoid Signaling," *Nature Neuroscience* 18 (2015): 75–86, https://doi.org/10.1038/nn.3892.

12. C. V. Rimoli, C. A. Valades-Cruz, V. Curcio, M. Mavrakis, and S. Brasselet, "4polar-STORM Polarized Super-resolution Imaging of Actin Filament Organization in Cells," *Nature Communications* 13 (2022): 301, https://doi.org/10.1038/s41467-022-27966-w.

13. F. V. Subach, G. H. Patterson, S. Manley, J. M. Gillette, J. Lippincott-Schwartz, and V. V. Verkhusha, "Photoactivatable mCherry for High-resolution Two-color Fluorescence Microscopy," *Nature Methods* 6 (2009): 153–159, https://doi.org/10.1038/nmeth.1298.

14. L. Xie, P. Dong, X. Chen, et al., "3D ATAC-PALM: Super-resolution Imaging of the Accessible Genome," *Nature Methods* 17 (2020): 430–436, https://doi.org/10.1038/s41592-020-0775-2.

15. S. Pujals and L. Albertazzi, "Super-resolution Microscopy for Nanomedicine Research," *ACS Nano* 13 (2019): 9707–9712, https://doi.org/10.1021/acsnano.9b05289.

16. T. Chen, B. Dong, K. Chen, et al., "Optical Super-Resolution Imaging of Surface Reactions," *Chemical Revision* 117 (2017): 7510–7537, https://doi.org/10.1021/acs.chemrev.6b00673.

17. L. Cognet, D. A. Tsyboulski, and R. B. Weisman, "Subdiffraction Far-field Imaging of Luminescent Single-walled Carbon Nanotubes," *Nano Letters* 8 (2008): 749–753, https://doi.org/10.1021/nl0725300.

18. G. Giannone, E. Hosy, F. Levet, et al., "Dynamic Superresolution Imaging of Endogenous Proteins on Living Cells at Ultra-high Density," *Biophysical Journal* 99 (2010): 1303–1310, https://doi.org/10.1016/j.bpj.2010.06.005.

19. R. Jungmann, C. Steinhauer, M. Scheible, A. Kuzyk, P. Tinnefeld, and F. C. Simmel, "Single-Molecule Kinetics and Super-Resolution Microscopy by Fluorescence Imaging of Transient Binding on DNA Origami," *Nano Letters* 10 (2010): 4756–4761, https://doi.org/10.1021/nl103427w.

20. H. H. Chen, G. J. Yan, M. H. Wen, et al., "Advancements and Practical Considerations for Biophysical Research: Navigating the Challenges and Future of Super-resolution Microscopy," *Chemical Biomedicine Imaging* 2 (2024): 331–344, https://doi.org/10.1021/cbmi.4c00019.

21. O. Rossier, V. Octeau, J. B. Sibarita, et al., "Integrins β1 and β3 Exhibit Distinct Dynamic Nanoscale Organizations inside Focal Adhesions," *Nature Cell Biology* 14 (2012): 1057–1067, https://doi.org/10.1038/ncb2588.

22. X. Yang, K. Zhanghao, H. Wang, et al., "Versatile Application of Fluorescent Quantum Dot Labels in Super-Resolution Fluorescence Microscopy," *ACS Photonics* 3 (2016): 1611–1618, https://doi.org/10.1021/acsphotonics.6b00178.

23. C. Werner, M. Sauer, and C. Geis, "Super-resolving Microscopy in Neuroscience," *Chemical Revision* 121 (2021): 11971–12015, https://doi.org/10.1021/acs.chemrev.0c01174.

24. A. G. Godin, B. Lounis, and L. Cognet, "Super-resolution Microscopy Approaches for Live Cell Imaging," *Biophysical Journal* 107 (2014): 1777–1784, https://doi.org/10.1016/j.bpj.2014.08.028.

25. C. J. R. Sheppard, *Encyclopedia of Modern Optics*, ed. R. D. Guenther (Elsevier, 2005), 61–69.

26. H. Deschout, F. Cella Zanacchi, M. Mlodzianoski, et al., "Precisely and Accurately Localizing Single Emitters in Fluorescence Microscopy," *Nature Methods* 11 (2014): 253–266, https://doi.org/10.1038/nmeth.2843.

27. E. Brooks Shera, N. K. Seitzinger, L. M. Davis, R. A. Keller, and S. A. Soper, "Detection of Single Fluorescent Molecules," *Chemical Physics Letters* 174 (1990): 553–557, https://doi.org/10.1016/0009-2614(90)85485-U.

28. K. R. Castleman and I. T. Young, *Microscope Image Processing*, 2nd ed., ed. F. A. Merchant and K. R. Castleman (Academic Press, 2023), 11–25.

29. A. J. Bard, *Electrogenerated Chemiluminescence* (CRC Press, 2004), https://doi.org/10.1201/9780203027011.

30. A. Zanut, A. Fiorani, S. Canola, et al., "Insights into the Mechanism of Coreactant Electrochemiluminescence Facilitating Enhanced Bioanalytical Performance," *Nature Communications* 11 (2020): 2668, https://doi.org/10.1038/s41467-020-16476-2.

31. X. R. Yang, J. M. Hang, W. Y. Qu, et al., "Gold Microbeads Enabled Proximity Electrochemiluminescence for Highly Sensitive and Size-Encoded Multiplex Immunoassays," *Journal of the American Chemical Society* 145 (2023): 16026–16036, https://doi.org/10.1021/jacs.3c04250.

32. W. L. Guo, H. Ding, C. Y. Gu, et al., "Potential-Resolved Multicolor Electrochemiluminescence for Multiplex Immunoassay in a Single Sample," *Journal of the American Chemical Society* 140 (2018): 15904–15915, https://doi.org/10.1021/jacs.8b09422.

33. P. Dutta, D. N. Han, B. Goudeau, D. C. Jiang, D. J. Fang, and N. Sojic, "Reactivity Mapping of Luminescence in Space: Insights into Heterogeneous Electrochemiluminescence Bioassays," *Biosensors & Bioelectronics* 165 (2020): 112372, https://doi.org/10.1016/j.bios.2020.112372.

34. G. Valenti, S. Scarabino, B. Goudeau, et al., "Single Cell Electrochemiluminescence Imaging: From the Proof-of-Concept to Disposable Device-Based Analysis," *Journal of the American Chemical Society* 139 (2017): 16830–16837, https://doi.org/10.1021/jacs.7b09260.

35. S. Voci, B. Goudeau, G. Valenti, et al., "Surface-Confined Electrochemiluminescence Microscopy of Cell Membranes," *Journal of the American Chemical Society* 140 (2018): 14753–14760.

36. B. Li, X. Huang, Y. Lu, et al., "High Electrochemiluminescence From Ru(bpy) 32+ Embedded Metal–Organic Frameworks to Visualize Single Molecule Movement at the Cellular Membrane," *Advancement of Science* 9 (2022): e2204715, https://doi.org/10.1002/advs.202204715.

37. C. Ma, S. J. Wu, Y. Zhou, et al., "Bio-Coreactant-Enhanced Electrochemiluminescence Microscopy of Intracellular Structure and Transport," *Angewandte Chemie International Edition* 60 (2021): 4907–4914.

38. C. Ma, M. X. Wang, H. F. Wei, et al., "Catalytic Route Electrochemiluminescence Microscopy of Cell Membranes With Nitrogen-doped Carbon Dots as Nano-coreactants," *Chemical Communications* 57 (2021): 2168–2171, https://doi.org/10.1039/D0CC08223F.

39. Y. Ma, C. Colin, J. Descamps, S. Arbault, and N. Sojic, "Shadow Electrochemiluminescence Microscopy of Single Mitochondria," *Angewandte Chemie International Edition* 60 (2021): 18742–18749.

40. J. Descamps, C. Colin, G. Tessier, S. Arbault, and N. Sojic, "Ultrasensitive Imaging of Cells and Sub-Cellular Entities by Electrochemiluminescence," *Angewandte Chemie International Edition* 62 (2023): e202218574.

41. K. Hiramoto, K. Ino, K. Komatsu, Y. Nashimoto, and H. Shiku, "Electrochemiluminescence Imaging of respiratory Activity of Cellular Spheroids Using Sequential Potential Steps," *Biosensors & Bioelectronics* 181 (2021): 113123, https://doi.org/10.1016/j.bios.2021.113123.

42. K. Hiramoto, K. Komatsu, R. Shikuwa, et al., "Evaluation of respiratory and Secretory Activities of Multicellular Spheroids via Electrochemiluminescence Imaging," *Electrochimica Acta* 458 (2023): 142507, https://doi.org/10.1016/j.electacta.2023.142507.

43. B. Li, Y. Lu, X. Huang, N. Sojic, D. Jiang, and B. Liu, "Stimuli-Responsive DNA Nanomachines for Intracellular Targeted Electrochemiluminescence Imaging in Single Cells," *Angewandte Chemie International Edition* 64 (2025): e202421658, https://doi.org/10.1002/anie.202421658.

44. Y. Liu, H. Zhang, B. Li, et al., "Single Biomolecule Imaging by Electrochemiluminescence," *Journal of the American Chemical Society* 143 (2021): 17910–17914, https://doi.org/10.1021/jacs.1c06673.

45. Y. Lu, X. Huang, S. Wang, B. Li, and B. Liu, "Nanoconfinement-Enhanced Electrochemiluminescence for In Situ Imaging of Single Biomolecules," *ACS Nano* 17 (2023): 3809–3817, https://doi.org/10.1021/acsnano.2c11934.

46. B. R. Layman and J. E. Dick, "Through-Space Electrochemiluminescence Reveals Bubble Forces at Remote Phase Boundaries," *Journal of the American Chemical Society* 146 (2024): 707–713, https://doi.org/10.1021/jacs.3c10505.

47. B. R. Layman and J. E. Dick, "Phase-Resolved Electrochemiluminescence with a Single Luminophore," *Journal of Physical Chemistry Letters* 14 (2023): 8151–8156, https://doi.org/10.1021/acs.jpclett.3c01993.

48. Y. Fu, B. Xie, M. Liu, et al., "Bipolar Electrochemiluminescence at the Water/Organic Interface," *Chemical Science* 15 (2024): 19907–19912, https://doi.org/10.1039/D4SC06103A.

49. S. Voci, T. B. Clarke, and J. E. Dick, "Abiotic Microcompartments Form When Neighbouring Droplets Fuse: An Electrochemiluminescence Investigation," *Chemical Science* 14 (2023): 2336–2341, https://doi.org/10.1039/D2SC06553C.

50. S. Voci and J. E. Dick, "An Electrochemical Perspective on the Interfacial Width between Two Immiscible Liquid Phases," *Current Opinion Electrochemical* 39 (2023): 101244, https://doi.org/10.1016/j.coelec.2023.101244.

51. Z. Xing, X. Gou, L. P. Jiang, J. J. Zhu, and C. Ma, "An In Situ Investigation of the Protein Corona Formation Kinetics of Single Nanomedicine Carriers by Self-Regulated Electrochemiluminescence Microscopy," *Angewandte Chemie International Edition* 62 (2023): e202308950.

52. S. Knezevic, J. Totoricaguena-Gorrino, R. K. R. Gajjala, et al., "Enhanced Electrochemiluminescence at the Gas/Liquid Interface of Bubbles Propelled into Solution," *Journal of the American Chemical Society* 146 (2024): 22724–22735, https://doi.org/10.1021/jacs.4c07566.

53. X. Huang, B. Li, Y. Lu, et al., "Direct Visualization of Nanoconfinement Effect on Nanoreactor via Electrochemiluminescence Microscopy," *Angewandte Chemie International Edition* 62 (2023): e202215078, https://doi.org/10.1002/anie.202215078.

54. M. J. Zhu, J. B. Pan, Z. Q. Wu, et al., "Electrogenerated Chemiluminescence Imaging of Electrocatalysis at a Single Au-Pt Janus Nanoparticle," *Angewandte Chemie International Edition* 57 (2018): 4010–4014, https://doi.org/10.1002/anie.201800706.

55. X. D. Gou, Z. J. Xing, C. Ma, and J. J. Zhu, "A Close Look at Mechanism, Application, and Opportunities of Electrochemiluminescence Microscopy," *Chemical Biomedicine Imaging* 1 (2023): 414–433, https://doi.org/10.1021/cbmi.2c00007.

56. Y. B. Vogel, C. W. Evans, M. Belotti, et al., "The Corona of a Surface Bubble Promotes Electrochemical Reactions," *Nature Communications* 11 (2020): 6323, https://doi.org/10.1038/s41467-020-20186-0.

57. S. Knežević, D. Han, B. Liu, D. Jiang, and N. Sojic, "Electrochemiluminescence Microscopy," *Angewandte Chemie International Edition* 63 (2024): e202407588.

58. S. F. Douman, E. Brennan, E. I. Iwuoha, and R. J. Forster, "Wireless Electrochemiluminescence at Nafion–Carbon Microparticle Composite Films," *Analytical Chemistry* 89 (2017): 11614–11619, https://doi.org/10.1021/acs.analchem.7b03040.

59. A. J. Wilson, K. Marchuk, and K. A. Willets, "Imaging Electrogenerated Chemiluminescence at Single Gold Nanowire Electrodes," *Nano Letters* 15 (2015): 6110–6115, https://doi.org/10.1021/acs.nanolett.5b02383.

60. J. Dong, Y. Lu, Y. Xu, et al., "Direct Imaging of Single-molecule Electrochemical Reactions in Solution," *Nature* 596 (2021): 244–249, https://doi.org/10.1038/s41586-021-03715-9.

61. J. R. Dong and J. D. Feng, "Electrochemiluminescence from Single Molecule to Imaging," *Analytical Chemistry* 95 (2023): 374–387, https://doi.org/10.1021/acs.analchem.2c04663.

62. J. Dong, Y. Xu, Z. Zhang, and J. Feng, "Operando Imaging of Chemical Activity on Gold Plates with Single-Molecule Electrochemiluminescence Microscopy," *Angewandte Chemie International Edition* 61 (2022): e202200187.

63. W. Zhu, J. Dong, G. Ruan, Y. Zhou, and J. Feng, "Quantitative Single-Molecule Electrochemiluminescence Bioassay," *Angewandte Chemie International Edition* 62 (2023): e202214419.

64. Y. Zhou, J. Dong, P. Zhao, J. Zhang, M. Zheng, and J. Feng, "Imaging of Single Bacteria with Electrochemiluminescence Microscopy," *Journal of the American Chemical Society* 145 (2023): 8947–8953, https://doi.org/10.1021/jacs.2c13369.

65. B. P. Lambert, H. Kerkhof, B. S. Flavel, and L. Cognet, "Morphology Determination of Luminescent Carbon Nanotubes by Analytical Super-Resolution Microscopy Approaches," *ACS Nano* 18 (2024): 30728–30736, https://doi.org/10.1021/acsnano.4c10025.

66. J. J. Zhang, D. Ye, C. H. Xu, et al., "Super-Resolved Mapping of Electrochemical Reactivity in Single 3D Catalysts," *Nano Letters* 25 (2025): 2074–2081.

67. M. M. Chen, C. H. Xu, W. Zhao, H. Y. Chen, and J. J. Xu, "Super-Resolution Electrogenerated Chemiluminescence Microscopy for Single-Nanocatalyst Imaging," *Journal of the American Chemical Society* 143 (2021): 18511–18518, https://doi.org/10.1021/jacs.1c07827.

68. S. Knezevic, E. Kerr, B. Goudeau, et al., "Bimodal Electrochemiluminescence Microscopy of Single Cells," *Analytical Chemistry* 95 (2023): 7372–7378.

69. Y. Yan, P. Zhou, L. Ding, et al., "T Cell Antigen Recognition and Discrimination by Electrochemiluminescence Imaging," *Angewandte Chemie International Edition* 62 (2023): e202314588.

70. H. Ding, P. Zhou, W. Fu, L. Ding, W. Guo, and B. Su, "Spatially Selective Imaging of Cell-Matrix and Cell-Cell Junctions by Electrochemiluminescence," *Angewandte Chemie International Edition* 60 (2021): 11769–11773.

71. H. Ding, W. Guo, and B. Su, "Imaging Cell-Matrix Adhesions and Collective Migration of Living Cells by Electrochemiluminescence Microscopy," *Angewandte Chemie International Edition* 59 (2020): 449–456, https://doi.org/10.1002/anie.201911190.

72. J. Tan, L. Xu, T. Li, B. Su, and J. Wu, "Image-Contrast Technology Based on the Electrochemiluminescence of Porous Silicon and Its Application in Fingerprint Visualization," *Angewandte Chemie International Edition* 53 (2014): 9822–9826, https://doi.org/10.1002/anie.201404948.

73. L. Xu, Y. Li, S. Wu, X. Liu, and B. Su, "Imaging Latent Fingerprints by Electrochemiluminescence," *Angewandte Chemie International Edition* 51 (2012): 8068–8072, https://doi.org/10.1002/anie.201203815.

74. M.-M. Chen, C.-H. Xu, W. Zhao, H.-Y. Chen, and J.-J. Xu, "Single Cell Imaging of Electrochemiluminescence-Driven Photodynamic Therapy," *Angewandte Chemie International Edition* 61 (2022): e202117401, https://doi.org/10.1002/anie.202117401.

75. H. Ding, W. Guo, and B. Su, "Imaging Cell-Matrix Adhesions and Collective Migration of Living Cells by Electrochemiluminescence Microscopy," *Angewandte Chemie International Edition* 59 (2020): 449–456, https://doi.org/10.1002/anie.201911190.

76. J. Tønnesen, V. Inavalli, and U. V. Nägerl, "Super-Resolution Imaging of the Extracellular Space in Living Brain Tissue," *Cell* 172 (2018): 1108–1121.e1115.

77. Y. M. Sigal, R. Zhou, and X. Zhuang, "Visualizing and Discovering Cellular Structures with Super-resolution Microscopy," *Science* 361 (2018): 880–887, https://doi.org/10.1126/science.aau1044.

78. A. Martinez-Marrades, J.-F. Rupprecht, M. Gross, and G. Tessier, "Stochastic 3D Optical Mapping by Holographic Localization of Brownian Scatterers," *Optics Express* 22 (2014): 29191, https://doi.org/10.1364/OE.22.029191.

79. U. V. Nägerl, K. I. Willig, B. Hein, S. W. Hell, and T. Bonhoeffer, "Live-cell Imaging of Dendritic Spines by STED Microscopy," *Pnas* 105 (2008): 18982–18987, https://doi.org/10.1073/pnas.0810028105.

80. N. T. Urban, K. I. Willig, S. W. Hell, and U. V. Nägerl, "STED Nanoscopy of Actin Dynamics in Synapses Deep inside Living Brain Slices," *Biophysical Journal* 101 (2011): 1277–1284, https://doi.org/10.1016/j.bpj.2011.07.027.

81. G. Valenti, A. Fiorani, H. D. Li, N. Sojic, and F. Paolucci, "Essential Role of Electrode Materials in Electrochemiluminescence Applications," *ChemElectroChem* 3 (2016): 1990–1997.

82. A. Jacassi, F. Tantussi, M. Dipalo, et al., "Scanning Probe Photonic Nanojet Lithography," *ACS Applied Material Interface* 9 (2017): 32386–32393.

83. H. Aouani, F. Deiss, J. Wenger, P. Ferrand, N. Sojic, and H. Rigneault, "Optical-fiber-microsphere for Remote Fluorescence Correlation Spectroscopy," *Optics Express* 17 (2009): 19085, https://doi.org/10.1364/OE.17.019085.

84. D. N. Han, D. C. Jiang, G. Valenti, et al., "Optics Determines the Electrochemiluminescence Signal of Bead-Based Immunoassays," *ACS Sensors* 8 (2023): 4782–4791.

85. H. M. Rodriguez, M. Martyniuk, K. S. Iyer, and S. Ciampi, "Insulator-on-Conductor Fouling Amplifies Aqueous Electrolysis Rates," *Journal of the American Chemical Society* 146 (2024): 10299–10311, https://doi.org/10.1021/jacs.3c11238.

86. R. Huang, M.-Y. Wei, and L.-H. Guo, "Enhanced Electrogenerated Chemiluminescence of /Tripropylamine System on Indium Tin Oxide Nanoparticle Modified Transparent Electrode," *Journal of Electroanalytical Chemistry* 656 (2011): 136–139, https://doi.org/10.1016/j.jelechem.2010.12.015.

87. N. Jayakumar and B. S. Ahluwalia, "From Superior Contrast to Super Resolution Label Free Optical Microscopy," *NPJ Imaging* 3 (2025): 1, https://doi.org/10.1038/s44303-024-00064-w.

88. J. M. Peter and H. A. Robert, "Signal-to-Noise Analysis of Various Imaging Systems," *ProcSPIE* 4259 (2001): 16–21.

89. C. Boncelet, *The Essential Guide to Image Processing* (Academic Press, 2009), 143–167.

90. L. Vizioli, S. Moeller, L. Dowdle, et al., "Lowering the Thermal Noise Barrier in Functional Brain Mapping with Magnetic Resonance Imaging," *Nature Communications* 12 (2021): 5181, https://doi.org/10.1038/s41467-021-25431-8.

91. X. Qinlan and C. Hong, "Image Denoising Based on Adaptive Filtering and Multi-frame Averaging," *AICI* 3 (2009): 523–526.

92. W. Guo, P. Zhou, L. Sun, H. Ding, and B. Su, "Microtube Electrodes for Imaging the Electrochemiluminescence Layer and Deciphering the Reaction Mechanism," *Angewandte Chemie International Edition* 60 (2021): 2089–2093, https://doi.org/10.1002/anie.202012340.

93. W. P. Kapuralage, H. Kala, M. Martyniuk, et al., "Stirring Without Stirrers: Polymer Fouling-Driven Mass Transport Unlocks Order-of-Magnitude Gain in Electrochemiluminescence," *Advancement of Science* 12 (2025): e06610, https://doi.org/10.1002/advs.202506610.

94. J. K. Leland and M. J. Powell, "Electrogenerated Chemiluminescence: An Oxidative-Reduction Type ECL Reaction Sequence Using Tripropyl Amine," *Journal of the Electrochemical Society* 137 (1990): 3127–3131, https://doi.org/10.1149/1.2086171.

Supporting Information

Additional supporting information can be found online in the Supporting Information section.

Supporting File 1: The authors have cited additional references within the Supporting Information [1–9].